

Exploring Differential Electron Transfer Kinetics of Electrochemical Aptamer-Based Sensors to Achieve Calibration-Free Measurements

Man Zhu, Chongyu Xie, Fan Xu, Shaoguang Li, Hui Li,* and Fan Xia

Cite This: *ACS Sens.* 2025, 10, 1105–1112

Read Online

ACCESS |



Metrics & More



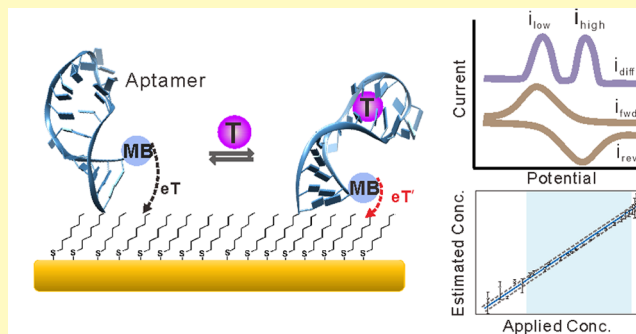
Article Recommendations



Supporting Information

ABSTRACT: Due to fabrication variation (i.e., device-to-device differences in the total number of probes immobilized on their electrode), electrochemical aptamer-based (EAB) sensors generally require calibration, reducing their convenience. In response, here, we describe an approach for achieving calibration-free EAB measurement relying on the differential electron transfer kinetics between target-bound and -unbound states using a square wave voltammetry technique. Specifically, by adjusting the amplitude and frequency of the potential wave, we generate a voltammetric output with two distinct current peaks, which are representative of signals probed from different electron transfer kinetics. The ratio of these two peaks provides a means of correcting the sensor-to-sensor fabrication variation. Using this approach, we demonstrate accurate, calibration-free measurements of multiple small molecules (e.g., kanamycin, ATP, and doxorubicin) and proteins (e.g., thrombin) in whole blood.

KEYWORDS: electrochemical, DNA aptamer, calibration-free measurements, peak split, square wave voltammetry



Electrochemical aptamer-based (EAB) sensors are a broad class of sensor platforms that we,^{1–3} and others,^{4–12} have demonstrated to support the measurement of a wide variety of target analytes. EAB sensors are comprised of a target-recognizing DNA or RNA aptamer that is covalently modified with the redox reporter at one terminus for signaling and with a thiol group at the other terminus as an anchoring group onto an interrogating electrode (Figure 1).¹³ Upon target binding, the aptamer changes its conformation and alters the electron transfer kinetics of the redox reporter,¹⁴ thus producing an easily measurable signal when the sensor is interrogated using square wave voltammetry (SWV) (Figure 1B). Due to such mechanism, EAB sensors are sensitive, specific, and selective directly being deployed in unprocessed clinical samples both in vitro^{1–3,5,7,11} and even in situ in the living body.^{8,10,15–17}

As is true for nearly all biosensors, EAB sensors require calibration to minimize sensor-to-sensor variations and achieve acceptable accuracy.^{1–4} In order to circumvent such variations and thus achieve calibration-free measurements, we have previously explored “dual-frequency” and “dual-reporter” strategies and achieved an accurate measurement for a variety of biorelevant molecules.^{1–3} The former relies on two individual measurements at a pair of responsive and non-responsive frequencies, which is a trade-off of time resolution, while the latter exploits a pair of redox reporters, requiring a sophisticated design in the structural modification of aptamer probes. Building on this, here, we describe a simple yet effective “dual-peak” approach to calibration-free EAB sensing, obviating the need to calibrate each individual sensor.

Specifically, by probing the electron transfer kinetics of a single redox reporter when the sensor is being interrogated using an optimized pair of frequency and amplitude, we can achieve differential forward and reverse electron transfer kinetics when using the SWV technique. Thus, we can generate two signals from each measurement, the ratio of which is greatly dependent on target concentrations, enabling calibration-free measurement of target molecules.

PRINCIPLE

Here, we employ the peak-splitting feature of square wave voltammetry to generate a dual signal output by using a signal redox-active molecule, enabling calibration-free measurements of target analytes. To achieve this goal, we demonstrate the principle in two steps: (1) the origin of the peak split and its rational manipulation; and (2) these two splitting peaks respond to the target to a different extent, which means one peak is responsive and the other is, if not at all, minimally responsive.

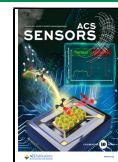
We use square wave voltammetry for sensor interrogation, in which a “staircase” rising potential waveform is applied to the

Received: October 23, 2024

Revised: December 22, 2024

Accepted: February 6, 2025

Published: February 12, 2025



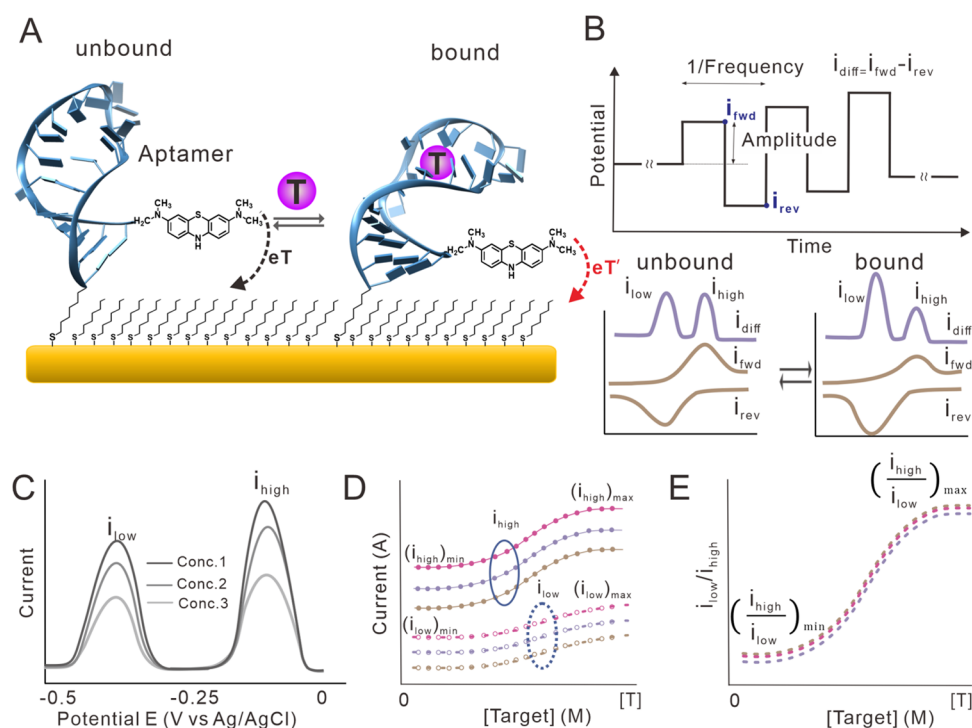


Figure 1. (A) Schematic of “dual-peak” EAB sensors. (B) Square wave voltammetry (SWV) is a technique in which each step is superimposed with a symmetrical double pulse, one of which is forward and the other is reversed. The current is collected at the end of each pulse (i_{fwd} and i_{rev}). By taking the difference between each measured current ($i_{\text{fwd}} - i_{\text{rev}}$), a voltammetry is generated.¹³ Because of this sampling protocol, SWV can be rationally manipulated to be more or less sensitive to specific electron transfer rates. (C) Absolute values of the two current peaks by EAB sensors vary dramatically among sensors due to variations in the electrode’s microscopic surface area and its aptamer packing density.¹ (D) We have exploited this effect to achieve calibration-free EAB measurements, relying on the different responses of the two peaks to the target analytes. (E) The ratio of these two signals ($i_{\text{low}}/i_{\text{high}}$) is reproducible for different sensors. The curves in three different colors (gray, pink, and blue) in (D) and (E) represent the results from three individual sensors.

sensor, and the Faradaic current is sequentially measured at the end of each square pulse (i.e., i_{fwd} and i_{rev} ; Figure 1B, upper panel). This generates forward and reverse current traces, the difference of which ($i_{\text{fwd}} - i_{\text{rev}}$) is the net voltammogram (i_{diff}). For the first step, the splitting peaks originate from the equilibrium between Ox(ads) and Red(ads) at the electrode surface (eq 1).^{18–28} When applying each potential pulse to the electrodes, the established equilibrium between these two species at the electrode surface will be disrupted, thus generating a flow of current that tends to restore such equilibrium. Achieving the new equilibrium requires additional energy, leading to a shift in both cathodic and anodic peaks in opposite directions (Figure 1B, unbound). As a consequence, this event results in a net peak split of voltammograms as the final output of redox transformations. The shapes of the voltammetric responses are a function of the kinetics and thermodynamics of the preceding chemical reaction, which can be rationally manipulated by altering the measurable parameters, such as square wave amplitude and frequencies.²⁹



As for the second step, upon target recognition, the sensors exhibited altered electron transfer kinetics in comparison to target-free unbound ones (Figure 1B, bound versus unbound), which can be probed by the forward or reverse sampling protocol. That is, the above two sampling protocols, one of which is more sensitive to the target, provide a higher signal response than the other. The splitting of the two peaks responds to the target analyte to different extents (Figure

1C,D), thus enabling them to achieve calibration-free measurements. Here, for example, the current peak at low potential (i_{low}) exhibits a more pronounced response against the target than the one at high potential (i_{high}).

As expected, the absolute currents at these two potentials are highly related to the total amount of DNA aptamer probes (and thus the MB reporter) on each electrode, thus varying significantly from sensor to sensor. In contrast, the ratio of these two currents is independent of the absolute amount of DNA probe; thus, taking this ratio eliminates such variation and enables calibration-free measurements (Figure 1E). Likewise, we can rationally manipulate the extent of peak splitting and the extent to which both peaks are responsive to the targets, again by tuning the amplitude and/or decreasing the SWV frequencies.

Upon demonstration of our hypothesis, we next derive how these peak splits achieve calibration-free measurements. Provided the aptamer binds one copy of its target, the relationship between the target concentration and voltammetric peak current, i , output by an EAB sensor is given by eq 2:²

$$[T] = K_D \frac{i - i_{\text{min}}}{i_{\text{max}} - i} \quad (2)$$

where K_D is the aptamer’s dissociation constant, and i_{min} and i_{max} are the peak currents that are observed in the absence of the target and in the presence of a saturating target, respectively. The former parameter, K_D , is constant for all sensors employing a given aptamer under a set of measurement

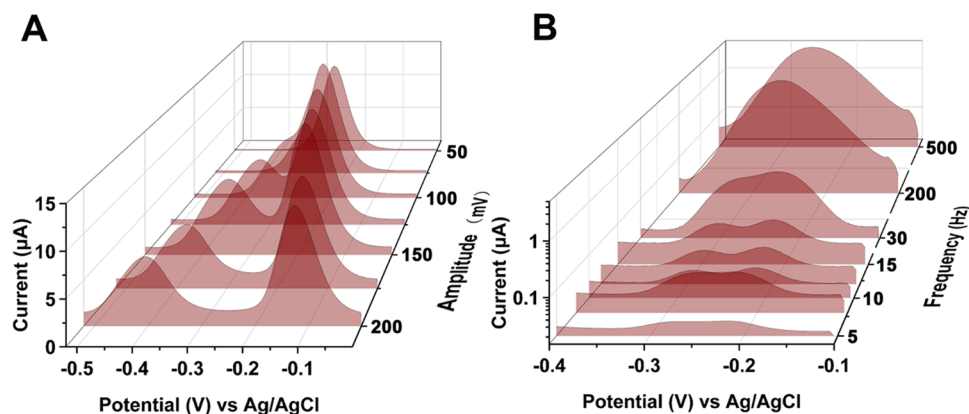


Figure 2. Three-dimensional voltammograms for kanamycin-detecting sensors deployed in PBS buffer. (A) At a fixed frequency of 60 Hz, we altered the amplitude from 50 to 200 mV, achieving a slight peak split at 80 mV (a shoulder peak is observed) before transitioning into well-separated peaks at ~100 mV. (B) When tuning the frequency at a fixed amplitude of 50 mV, we observed a peak split only at low frequencies (e.g., 5 Hz), with higher frequencies exhibiting a broad peak.

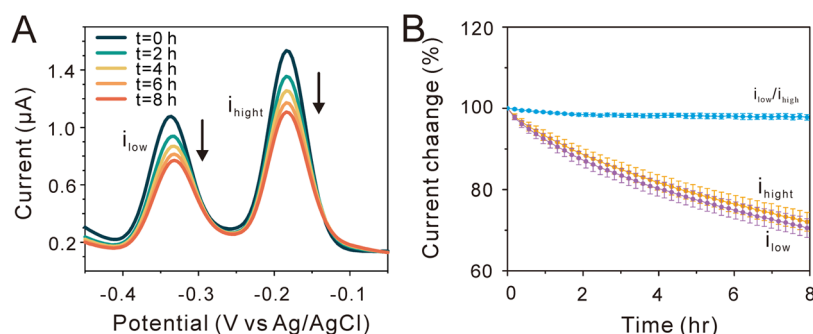


Figure 3. The “dual-peak” strategy enables our sensors to achieve high stability by taking the ratio of currents at high and low potentials. (A) SWV voltammograms of kanamycin-detecting sensors during the stability test. (B) Although both currents at high and low potentials are degrading (orange and purple traces), their ratios are quite stable with less than 5% variation (blue trace). The error bars displayed in panel (B) indicate the standard deviations of the three independently hand-fabricated sensors.

conditions. In contrast, the parameters i_{\min} and i_{\max} however, vary dramatically from one individual sensor to the next due to significant variations in the microscopic surface area of the sensing electrode and the density with which the reporter-modified aptamers are packed onto it. This variation is so great that we cannot derive target concentrations from measurements of the peak current alone (Figure 1C,D). Fortunately, however, the relative EAB signal change (e.g., i/i_{\min}) is well correlated with the target concentration, irrespective of the sensor-to-sensor variation in i_{\min} . The ratio of i_{\max} to i_{\min} , which is the sensor's gain (denoted here as γ), is likewise constant (Figure 1C) and, thus, eq 2 simplifies to eq 3 [ref 2]:

$$[T] = K_D \frac{i - i_{\min}}{i_{\min} \times \gamma - i} \quad (3)$$

When the sensor is interrogated and exhibits dual peaks, we can employ either the peak current for measurements. Here, for example, we use the peak current at a lower potential, i_{low} and then eq 2 is written as

$$[T] = K_D \frac{i_{\text{low}} - (i_{\text{low}})_{\min}}{(i_{\text{low}})_{\min} \times \gamma - i_{\text{low}}} \quad (4)$$

We then introduce a second peak current (e.g., i_{high}) by dividing the numerator and denominator by i_{high} . Due to the two peaks originating from the same reporter, the minimal value at the baseline of the ratio of i_{low} to i_{high} is also constant

irrespective of the total probe amount, here denoted as α . Then, we can derive eq 4 as the following formula, which is simplified into a relationship between the target concentration and the ratio of i_{low} to i_{high} .

$$[T] = K_D \frac{\frac{i_{\text{low}}}{i_{\text{high}}} - \left(\frac{i_{\text{low}}}{i_{\text{high}}}\right)_{\min}}{\left(\frac{i_{\text{low}}}{i_{\text{high}}}\right)_{\min} \times \gamma - \frac{i_{\text{low}}}{i_{\text{high}}}} = K_D \frac{\frac{i_{\text{low}}}{i_{\text{high}}} - \alpha}{\alpha \times \gamma - \frac{i_{\text{low}}}{i_{\text{high}}}} \quad (5)$$

From this, we see that the target concentration is related to five parameters, two of which, i_{low} and i_{high} , are the sensor outputs in the sample, and three more, α , γ , and K_D , are constants only required to be determined once during the original design and validation of a given type of sensor, rather than for each individual sensor. Thus, we can use the $i_{\text{low}}/i_{\text{high}}$ ratio to determine the target concentrations accurately and precisely via a relationship (eq 5).

We employed this “dual-peak” calibration-free approach for a kanamycin-detecting EAB sensor. To do so, we first optimized the amplitude/frequency pair that supports the achievement of well-splitting peaks and we tested this orthogonal pair of parameters across different matrices, as demonstrated by the experimental results (Table S3). As expected, sensors exhibit splitting peaks at higher amplitudes or lower frequencies, with changes in amplitude having a pronounced effect on peak splitting.²² For example, at a

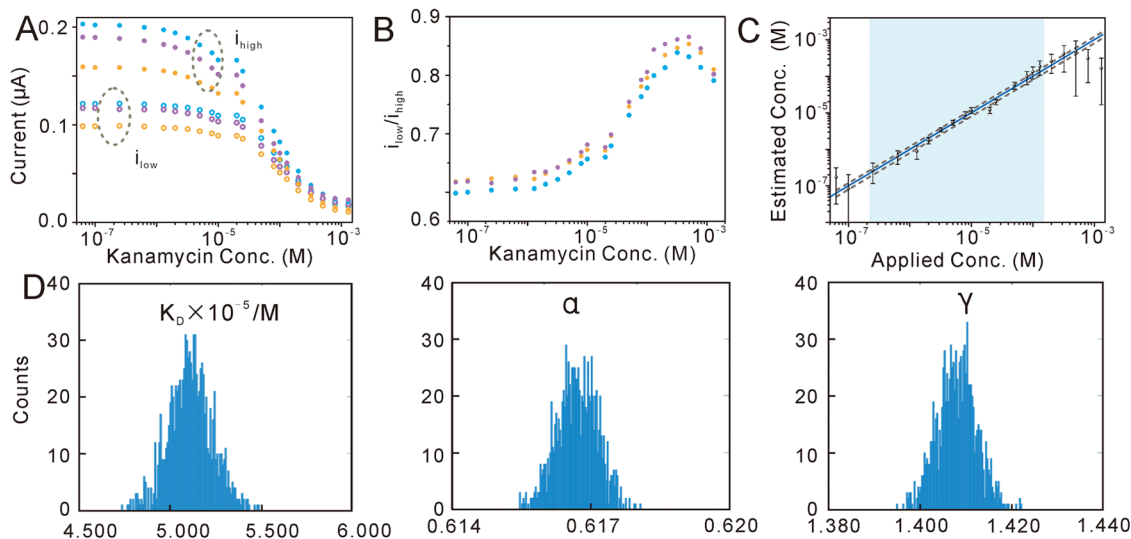


Figure 4. We achieved calibration-free measurements for kanamycin-detecting sensors in PBS. (A) First, we challenged a set of a single-reporter, kanamycin-detecting sensors in PBS buffer, visibly observing significant variation in i_{low} and i_{high} . (B) However, the ratio of i_{low} to i_{high} is quite reproducible. (C) Finally, we recover kanamycin concentration estimates over a 600-fold concentration range from 2.5×10^{-7} to 1.5×10^{-4} M in PBS. (D) Optimized parameters obtained via global fitting. The squared errors in the fittings (Figure S3) were propagated by Monte Carlo analysis in order to provide a distribution of the variability in the calculated parameters K_D , α , and γ . The dashed lines in panel (C) represent the $\pm 20\%$ accuracy bands. The different color curves in (A) and (B) represent the test results of the different sensors. The error bars displayed in (C) and the following figures indicate the standard deviation of the three independent hand-fabricated sensors.

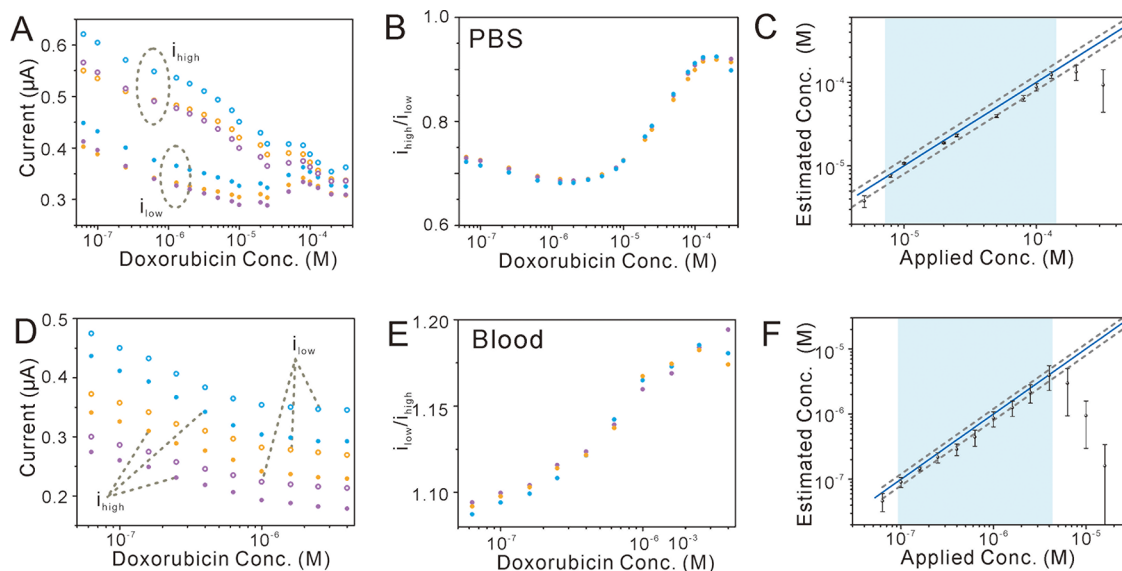


Figure 5. We achieved calibration-free measurements for doxorubicin-detecting sensors in PBS and whole blood. (A) A set of single-reporter, doxorubicin-detecting sensors was challenged in PBS. It was clearly observed that the i_{low} and i_{high} vary dramatically in different sensors. (B) Conversely, i_{high}/i_{low} was quite reproducible. (C) Specifically, this single-reporter, dual-peak, calibration-free approach produces doxorubicin concentration in PBS and estimates the actual concentration from 7.9×10^{-6} to 1.3×10^{-4} M, achieving a concentration range of approximately 16.5-fold. (D) We prepared a new set of doxorubicin-detecting sensors and challenged them in whole blood samples. As expected, the i_{low} and i_{high} vary dramatically in different sensors. (E) Conversely, i_{low}/i_{high} was quite reproducible. (F) Specifically, this calibration-free approach produces doxorubicin concentration in whole blood that estimates the actual concentration from 1.0×10^{-7} to 4.0×10^{-6} M, achieving an approximately 40-fold concentration range. The dashed lines in (C) and (F) represent the $\pm 20\%$ accuracy bands. The different color curves in (A–E) represent the test results of the different sensors.

frequency of 60 Hz, as the amplitudes increase from 50 to 200 mV, the peak begins to split at 80 mV (a shoulder peak is seen) before transitioning into well-separated peaks ~ 100 mV (Figures 2A and S1). In parallel, at an amplitude of 50 mV, when decreasing the frequency down to 5–10 Hz (Figure 2B), we observed a splitting peak coupled with a lower absolute current value. Finally, we obtained an optimized pair of

amplitude and frequency for the well-resolved peak splits at an amplitude of 50 mV and a frequency of 15 Hz. The amplitude/frequency pair of all of the sensors employed in this study was optimized across different matrices, as demonstrated by the experimental results (Tables S3–S10). The final selected test parameters for the data of all the systems discussed in this paper are summarized in Table S11.

Using this pair of parameters, we then tested the signal stability of kanamycin-recognizing sensors in a buffer in a continuous, real-time fashion over a period of 8 h. While both current signals at low and high potentials were degraded by 30%, we achieved excellent signaling stability for these sensors using the ratio of these two currents with less than 5% variations in the signals (Figure 3).

Next, we then challenged kanamycin-recognizing sensors in a buffer with increasing concentrations of the target while interrogating them under this condition to generate titration data. Because these two peaks are generated from the same reporter on each electrode, their absolute currents depend on the total amount of DNA molecules on the surface and thus vary from sensor to sensor due to fabrication variations (Figure 4A), while the values of $i_{\text{low}}/i_{\text{high}}$ are quite reproducible (Figure 4B). We globally fit these titration data to eq 4 to determine α , γ , and K_D (Figures 4D and S4 and Table S1). Finally, applying these parameters to another set of sensors, we recover kanamycin concentration estimates within a 20% error of the spiked concentrations over a 600-fold concentration range from 2.5×10^{-7} to 1.5×10^{-4} M (Figure 4C). Motivated by the promising results in simple buffers, we then challenged these sensors in whole blood with increasing concentrations of the target. Once again, while these two peak signals vary significantly across different sensors (Figure S5A), the values of $i_{\text{low}}/i_{\text{high}}$ are quite reproducible (Figure S5B). After globally fitting these titration data to eq 4 to determine α , γ , and K_D (Figures S4D and S5 and Table S2), and applying these parameters to a new set of sensors, we recover kanamycin concentration estimates over a 405-fold concentration range from 7.9×10^{-6} to 3.2×10^{-3} M within 20% error of the spiked concentrations (Figure S5C).

Motivated by this observation of EAB sensors against kanamycin, we also verify their application to other small molecules, including doxorubicin (DOX) and ATP. First, we tested our doxorubicin-detecting sensors and we challenged a training set of sensors with increasing concentrations of doxorubicin to generate the titration data. Similarly, we observed that with the increase of target concentrations, the absolute current signal for both the low potential peak and the high potential peak decreases at concert, and both signals vary significantly from one sensor to the next (Figure 5A). Remarkably, the ratio $i_{\text{high}}/i_{\text{low}}$ is quite reproducible (Figure 5B). We globally fit this data set to eq 4 to determine α , γ , and K_D (Figures S7 and S8 and Table S1). Using these parameters, we applied them to another set of testing sensors, producing doxorubicin concentration in PBS that estimates the actual concentration from 7.9×10^{-6} to 1.3×10^{-4} M within $\pm 20\%$ of the actual concentration, achieving a concentration range of approximately 16.5-fold (Figure 5C). When deployed in whole blood, the doxorubicin-detecting sensors likewise achieved good reproducibility using the ratio of these two peaks (Figure 5D,E). Once again, we first obtained a set of titration data under the optimal parameters and globally fit to eq 4 to determine α , γ , and K_D (Figures S9 and S10 and Table S2), producing doxorubicin concentration in whole blood that estimates the actual concentration from 1.0×10^{-7} to 4.0×10^{-6} M within $\pm 20\%$ of the actual concentration, achieving an approximate 40-fold concentration range (Figure 5F). The stability of the doxorubicin-detecting sensors was experimentally determined and is presented in Figures S2C and S3C. The results show that the ratio signal has excellent stability.

We further verify the dual-peak calibration-free approach, enabling the measurement of ATP using our ATP-detecting sensors. Similarly, we observed that with the increase of ATP concentrations, the absolute current signal for both the low potential peak and the high potential peak decreases at concert, and both signals vary significantly from one sensor to the next (Figure S15A). Remarkably, the ratio $i_{\text{low}}/i_{\text{high}}$ is quite reproducible (Figure S15B). We globally fit this data set to eq 4 to determine α , γ , and K_D (Figures S11 and S12 and Table S1). Using these parameters, we applied them to another set of testing sensors, producing ATP concentration in PBS that estimates the actual concentration over 31.7-fold from 6.3×10^{-8} to 2.0×10^{-6} M within $\pm 20\%$ of the actual concentration (Figure S15C). When deployed in whole blood, the ATP-detecting sensors likewise achieved good reproducibility using the ratio of these two peaks (Figure S15D,E). The globally fitted data are shown in Figures S13 and S14 and Table S2. Using a dual-peak calibration-free approach, our sensor produced ATP concentration in whole blood that estimates the actual concentration over 6.25-fold from 8.0×10^{-5} to 5.0×10^{-4} M within $\pm 20\%$ of the actual concentration (Figure S15F). The stability of the ATP-detecting sensors was also verified by experiments, and the results are shown in Figures S2B and S3B. The experimental results show that the peak current of the high potential and low potential in the sensor decreases obviously with the progress of the test, while the ratio signal remains stable.

In order to verify the generality of our dual-peak approach toward target types other than small molecules, we further applied it for the detection of protein analytes. Here, we employed a thrombin-recognizing aptamer to fabricate its EAB sensors.^{5,30,31} We globally fit these titration data to eq 4 for the determination of α , γ , and K_D (Figures S16 and S17 and Table S1). By applying these parameters to another set of testing sensors, we recover thrombin concentration estimates within $\pm 20\%$ of the actual concentration over 2.8-fold from 3.6×10^{-7} to 1.0×10^{-6} M (Figure S18C). Likewise, we titrated a set of training sensors in Tris buffer, once again observing that while the currents produced by the two peaks vary dramatically from sensor to sensor, the $i_{\text{high}}/i_{\text{low}}$ values are quite reproducible (Figure S18A,B).

The dual-peak calibration-free approach likewise holds for thrombin detection in a complex matrix. Due to its intrinsic properties, such as its role in blood coagulation, thrombin causes blood clotting when applying our sensors directly to whole blood, failing the measurements. Therefore, we challenged our thrombin EAB sensors in 50% diluted blood serum. Again, while both peaks vary significantly from one sensor to the next, the $i_{\text{low}}/i_{\text{high}}$ values are reproducible. After obtaining α , γ , and K_D by global fitting (Figures S19 and S20 and Table S2), we recovered thrombin concentration estimates within $\pm 20\%$ of the actual concentration over 4.5-fold from 8.0×10^{-8} to 3.6×10^{-7} M (Figure S18F).

Similarly, the stability of the thrombin-detecting sensors was evaluated experimentally prior to the titration test, with the corresponding results depicted in Figures S2D and S3D. It is evident from the figures that the stability of both the high and low potential peak currents in the sensors is significantly less robust than that of the ratio signal.

To further test the scope of dual-peak calibration-free EAB sensing, we also challenged both kanamycin- and doxorubicin-detecting sensors in flowing whole blood. Under these challenging conditions, the currents generated by kanamycin-

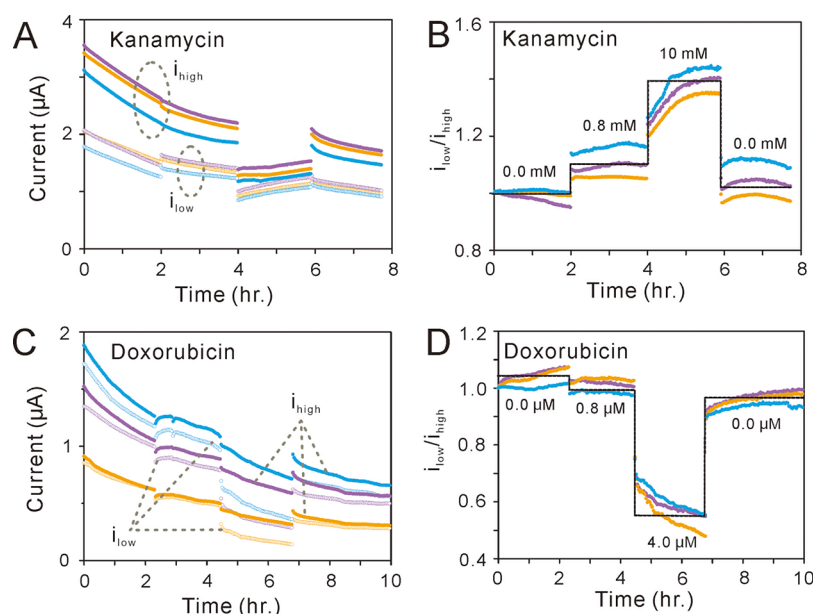


Figure 6. Calibration-free measurement of doxorubicin and kanamycin in whole blood sample. When challenged in vitro in undiluted whole blood, the absolute peak currents of the two peaks of kanamycin-detecting (A) and doxorubicin-detecting (C) sensors vary dramatically in different sensors. Comparing the 1st and 7th hour baselines (0.0 mM target) for individual sensors, it is not difficult to find that there is a significant difference within individual sensors. (B) Even under these demanding conditions, the dual-peak calibration-free sensors are reproducible, and the baselines (0.0 mM target) of the sensors are well recovered after all kanamycin has been cleaned. (D) Doxorubicin (DOX) detection sensors show a similar phenomenon when challenged in undiluted whole blood. The different colored curves represent the test results of the different sensors.

detecting sensors vary significantly from one sensor to the next, with more significant signal drifts observed for a single sensor over the course of a couple of hours (Figure 6A). After correction using eq 4, however, we obtained stable, distinguishable signals when applying different concentrations and a good return to baseline (Figure 6B). When the ratio signal was converted to the target concentration, an evident administration step remained observable despite a certain discrepancy between the measured and actual concentrations (Figure S21A).

We further challenged doxorubicin-detecting sensors in the whole blood. Once again, the currents generated by doxorubicin-detecting sensors vary significantly from one sensor to the next, with more significant signal drifts observed for a single sensor over the course of a couple of hours (Figure 6C). After correction using eq 4, however, we obtained stable, distinguishable signals when applying different concentrations and a good return to baseline (Figures 6D and S21B). Similarly, when the ratio signal is converted to the target concentration, an evident administration step is observed despite some differences between the measured and actual concentrations (Figure S21B).

CONCLUSIONS

Here, we demonstrate a method to achieve the double peak of a single signal reporter by changing the test parameters (amplitude and frequency) and using the ratio of the two peaks as the signal output to achieve calibration-free measurements in whole blood. Using this method, we estimate target concentration for three kinds of small molecules (kanamycin, ATP, and doxorubicin) within $\pm 20\%$ of the spiked target concentration across concentration ranges of 6.25- to 405-fold in whole blood and 16.5- to 600-fold in PBS. For the protein (thrombin), we estimate a target concentration within $\pm 20\%$ of the actual concentration over 2.8-fold from 3.6×10^{-7} to 1.0

$\times 10^{-6}$ M in Tris buffer and over 4.5-fold from 8.0×10^{-8} to 3.6×10^{-7} M in 50% diluted blood serum. Meanwhile, we also used this method to perform continuous measurements of kanamycin and doxorubicin in flowing, undiluted whole blood over the course of many hours, again achieving good accuracy and precision despite the significant drift seen in the absolute sensor current under these more challenging conditions. This measurement provides a convenient, single-step approach to the measurement of specific small molecules and proteins in buffer solutions and challenging conditions such as whole blood and blood serum.

This strategy is simple and cost-effective. Therefore, we believe that the described approach may broadly improve the utility of EAB sensors. Furthermore, this method can be applied to any folding-based sensor, which utilizes the change in the electron transfer rate of electrochemical signal molecules as the output signal such as E-DNA sensors^{32–36} and PNA-based biosensors.^{37–41} Our dual-peak, calibration-free approach is general, as the specificity of EAB sensors can be transformed by simply replacing its aptamer.^{41–50} Moreover, this method is expected to achieve accurate, rapid, and real-time detection of drug concentration in vivo and achieve in situ, high spatiotemporal resolution pharmacokinetic analysis.

ASSOCIATED CONTENT

Supporting Information

The Supporting Information is available free of charge at <https://pubs.acs.org/doi/10.1021/acssensors.4c02953>.

Pharmaceuticals utilized, aptamer sequences, procedures for electrode cleaning, methodologies for sensor preparation, electrochemical measurement conditions for sensors, stability assessment results of various sensors, global fitting graphs, and distribution of the variability in the calculated parameters of the sensors, etc. (PDF)

AUTHOR INFORMATION

Corresponding Author

Hui Li – State Key Laboratory of Geomicrobiology and Environmental Changes, Engineering Research Center of Nano-Geomaterials of Ministry of Education, Faculty of Materials Science and Chemistry, China University of Geosciences, Wuhan 430074, P. R. China; orcid.org/0000-0001-7849-9735; Email: lihui-chem@cug.edu.cn

Authors

Man Zhu – Faculty of Materials Science and Engineering, Hubei Polytechnic University, Huangshi 435003 Hubei, P. R. China; State Key Laboratory of Geomicrobiology and Environmental Changes, Engineering Research Center of Nano-Geomaterials of Ministry of Education, Faculty of Materials Science and Chemistry, China University of Geosciences, Wuhan 430074, P. R. China

Chongyu Xie – State Key Laboratory of Geomicrobiology and Environmental Changes, Engineering Research Center of Nano-Geomaterials of Ministry of Education, Faculty of Materials Science and Chemistry, China University of Geosciences, Wuhan 430074, P. R. China

Fan Xu – State Key Laboratory of Geomicrobiology and Environmental Changes, Engineering Research Center of Nano-Geomaterials of Ministry of Education, Faculty of Materials Science and Chemistry, China University of Geosciences, Wuhan 430074, P. R. China

Shaoguang Li – State Key Laboratory of Geomicrobiology and Environmental Changes, Engineering Research Center of Nano-Geomaterials of Ministry of Education, Faculty of Materials Science and Chemistry, China University of Geosciences, Wuhan 430074, P. R. China

Fan Xia – State Key Laboratory of Geomicrobiology and Environmental Changes, Engineering Research Center of Nano-Geomaterials of Ministry of Education, Faculty of Materials Science and Chemistry, China University of Geosciences, Wuhan 430074, P. R. China; orcid.org/0000-0001-7705-4638

Complete contact information is available at:

<https://pubs.acs.org/10.1021/acssensors.4c02953>

Notes

The authors declare no competing financial interest.

ACKNOWLEDGMENTS

This work was supported by the National Natural Science Foundation of China (22474130, 22274144, 22090050), the National Key Research and Development Program of China (2021YFA1200403), the Joint NSFC-ISF Research Grant Program (Grant No. 22161142020), and the Natural Science Foundation of Shenzhen (JCYJ20220530162406014). We would like to acknowledge Prof. Dr. Philippe Dauphin-Ducharme for helpful discussions on the optimization of the testing parameters.

REFERENCES

- (1) Zhu, M.; Li, S.; Li, H.; Li, H.; Xia, F. Employing an Intercalated Redox Reporter in Electrochemical Aptamer-Based Biosensors to Enable Calibration-Free Molecular Measurements in Undiluted Serum. *Anal. Chem.* **2020**, *92*, 12437–12441.
- (2) Li, H.; Dauphin-Ducharme, P.; Ortega, G.; Plaxco, K. W. Calibration-Free Electrochemical Biosensors Supporting Accurate Molecular Measurements Directly in Undiluted Whole Blood. *J. Am. Chem. Soc.* **2017**, *139*, 11207–11213.
- (3) Li, H.; Arroyo-Curras, N.; Kang, D.; Ricci, F.; Plaxco, K. W. Dual-Reporter Drift Correction to Enhance the Performance of Electrochemical Aptamer-Based Sensors in Whole Blood. *J. Am. Chem. Soc.* **2016**, *138*, 15809–15812.
- (4) Ma, R.-N.; Wang, L.-L.; Wang, H.-F.; Jia, L.-P.; Zhang, W.; Shang, L.; Xue, Q.-W.; Jia, W.-L.; Liu, Q.-Y.; Wang, H.-S. Highly Sensitive Ratiometric Electrochemical DNA Biosensor Based on Homogeneous Exonuclease Iii-Assisted Target Recycling Amplification and One-Step Triggered Dual-Signal Output. *Sens. Actuators, B* **2018**, *269*, 173–179.
- (5) Xiao, Y.; Lubin, A. A.; Heeger, A. J.; Plaxco, K. W. Label-Free Electronic Detection of Thrombin in Blood Serum by Using an Aptamer-Based Sensor. *Angew. Chem., Int. Ed.* **2005**, *44*, 5456–5469.
- (6) Radi, A.-E.; Acero Sánchez, J. L.; Baldrich, E.; O'Sullivan, C. K. Reagentless, Reusable, Ultrasensitive Electrochemical Molecular Beacon Aptasensor. *J. Am. Chem. Soc.* **2006**, *128*, 117–124.
- (7) Zhao, G.; Liu, Y.; Du, J.; Zhang, H.; Feng, H.; Lu, X. Application of Tetrahedral-Deoxyribonucleic Acid Electrochemistry Platform Coupling Aptazymes and Hybridized Hairpin Reactions for the Measurement of Extracellular Adenosine Triphosphate in Plants. *Anal. Chim. Acta* **2021**, *1172*, 338681.
- (8) Sun, L.; Shen, F.; Tian, L.; Tao, H.; Xiong, Z.; Xu, J.; Liu, Z. Atp-Responsive Smart Hydrogel Releasing Immune Adjuvant Synchronized with Repeated Chemotherapy or Radiotherapy to Boost Antitumor Immunity. *Adv. Mater.* **2021**, *33*, 2007910.
- (9) Jia, W.; Xie, D.; Li, F.; Wu, X.; Wang, R.; Yang, L.; Liu, L.; Yin, W.; Chang, S. Evaluation the Effect of Nanoparticles on the Structure of Aptamers by Analyzing the Recognition Dynamics of Aptamer Functionalized Nanoparticles. *Anal. Chim. Acta* **2021**, *1183*, 338976.
- (10) Liu, Y.; Yan, J.; Howland, M. C.; Kwa, T.; Revzin, A. Micropatterned Aptasensors for Continuous Monitoring of Cytokine Release from Human Leukocytes. *Anal. Chem.* **2011**, *83*, 8286–8292.
- (11) Ferapontova, E. E.; Olsen, E. M.; Gothelf, K. V. An Rna Aptamer-Based Electrochemical Biosensor for Detection of Theophylline in Serum. *J. Am. Chem. Soc.* **2008**, *130*, 4256–4258.
- (12) Zuo, X.; Song, S.; Zhang, J.; Pan, D.; Wang, L.; Fan, C. A Target-Responsive Electrochemical Aptamer Switch (Treas) for Reagentless Detection of Nanomolar Atp. *J. Am. Chem. Soc.* **2007**, *129*, 1042–1043.
- (13) Bard, A. J.; Faulkner, L. R. *Electrochemical Methods – Fundamentals and Applications*; John Wiley & Sons, Inc.: New York pp 293–299.
- (14) Dauphin-Ducharme, P.; Plaxco, K. W. Maximizing the Signal Gain of Electrochemical-DNA Sensors. *Anal. Chem.* **2016**, *88*, 11654–11662.
- (15) Arroyo-Currás, N.; Ortega, G.; Copp, D. A.; Ploense, K. L.; Plaxco, Z. A.; Kippin, T. E.; Hespanha, J. P.; Plaxco, K. W. High-Precision Control of Plasma Drug Levels Using Feedback-Controlled Dosing. *ACS Pharmacol. Transl. Sci.* **2018**, *1*, 110–118.
- (16) Arroyo-Currás, N.; Scida, K.; Ploense, K. L.; Kippin, T. E.; Plaxco, K. W. High Surface Area Electrodes Generated Via Electrochemical Roughening Improve the Signaling of Electrochemical Aptamer-Based Biosensors. *Anal. Chem.* **2017**, *89*, 12185–12191.
- (17) Idili, A.; Arroyo-Curras, N.; Ploense, K. L.; Csordas, A. T.; Kuwahara, M.; Kippin, T. E.; Plaxco, K. W. Seconds-Resolved Pharmacokinetic Measurements of the Chemotherapeutic Irinotecan in Situ in the Living Body. *Chem. Sci.* **2019**, *10*, 8164–8170.
- (18) Fatouros, N.; Krulic, D.; Larabi, N. Forward and Reverse Scans in Square Wave Voltammetry Applied to the First Order Ce Mechanism. *J. Electroanal. Chem.* **2003**, *549*, 81–90.
- (19) Doménech-Carbó, A.; Martini, M.; de Carvalho, L. M.; Doménech-Carbó, M. T. Square Wave Voltammetric Determination of the Redox State of a Reversibly Oxidized/Reduced Depolarizer in Solution and in Solid State. *J. Electroanal. Chem.* **2012**, *684*, 13–19.
- (20) Son, K.; Uzawa, T.; Ito, Y.; Kippin, T.; Plaxco, K. W.; Fujie, T. Survey of Oligoethylene Glycol-Based Self-Assembled Monolayers on

Electrochemical Aptamer-Based Sensor in Biological Fluids. *Biochem. Biophys. Res. Commun.* **2023**, *668*, 1–7.

(21) Mirčeski, V.; Lovrić, M. Split Square-Wave Voltammograms of Surface Redox Reactions. *Electroanalysis* **1997**, *9*, 1283–1287.

(22) Lovrić, M.; Komorsky-Lovric, S. Square-Wave Voltammetry of an Adsorbed Reactant. *J. Electroanal. Chem. Interfacial Electrochem.* **1988**, *248*, 239–253.

(23) Andreev, E. A.; Borisov, D. E.; Karyakin, A. A. Square-Wave Voltammetric Evaluation of Electrochemical Constants: Comparative Study with Other Techniques. *J. Electroanal. Chem.* **2024**, *957*, No. 118134.

(24) Gulaboski, R. The Net Peak Splitting Phenomenon in Square-Wave Voltammetry – a Simple Diagnostic Tool to Distinguish between Surface Electrode Mechanisms Associated with Different Chemical Reactions. *Maced. J. Chem. Chem. Eng.* **2023**, *42*, 237–247.

(25) Mirčeski, V. Charge Transfer Kinetics in Thin-Film Voltammetry. Theoretical Study under Conditions of Square-Wave Voltammetry. *J. Phys. Chem. B* **2004**, *108*, 13719–13725.

(26) Mirčeski, V.; Lovric, M. Square-Wave Voltammetry of a Cathodic Stripping Reaction Complicated by Adsorption of the Reacting Ligand. *Anal. Chim. Acta* **1999**, *386*, 47–62.

(27) O'Dea, J. J.; Osteryoung, J. G. Characterization of Quasi-Reversible Surface Processes by Square-Wave Voltammetry. *Anal. Chem.* **1993**, *65*, 3090–3097.

(28) Molina, P. G.; Zón, M. A.; Fernández, H. The Redox Kinetics of Adsorbed Atx-I at Carbon Electrodes by Anodic Stripping Square-Wave Voltammetry. *Electroanalysis* **2000**, *12*, 791–798.

(29) Gulaboski, R.; Mirčeski, V.; Lovrić, M.; Bogeski, I. Theoretical Study of a Surface Electrode Reaction Preceded by a Homogeneous Chemical Reaction under Conditions of Square-Wave Voltammetry. *Electrochem. Commun.* **2005**, *7*, 515–522.

(30) Goda, T.; Higashi, D.; Matsumoto, A.; Hoshi, T.; Sawaguchi, T.; Miyahara, Y. J Am Chem Soc Dual Aptamer-Immobilized Surfaces for Improved Affinity through Multiple Target Binding in Potentiometric Thrombin Biosensing. *Biosens. Bioelectron.* **2015**, *73*, 174–180.

(31) Xiao, Y.; Piorek, B. D.; Plaxco, K. W.; Heeger, A. J. A Reagentless Signal-on Architecture for Electronic, Aptamer-Based Sensors Via Target-Induced Strand Displacement. *J. Am. Chem. Soc.* **2005**, *127*, 17990–17991.

(32) Khaliliazar, S.; Oberg Mansson, I.; Piper, A.; Ouyang, L.; Reu, P.; Hamed, M. M. Woven Electroanalytical Biosensor for Nucleic Acid Amplification Tests. *Adv. Healthcare Mater.* **2021**, *10*, 2100034.

(33) Cao, H. T.; Pham, X. T. T.; Ha, V. L.; Le, V. H. Effectiveness of Hairpin Probe in Increasing the Limit of Detection for Gold Nanowire Based-Biosensor. *Adv. Nat. Sci.: Nanosci. Nanotechnol.* **2014**, *5*, 045017.

(34) Daniel, J.; Fetter, L.; Jett, S.; Rowland, T. J.; Bonham, A. J. Electrochemical Aptamer Scaffold Biosensors for Detection of Botulism and Ricin Proteins. *Methods Mol. Biol.* **2017**, *1600*, 9–23.

(35) Salimian, R.; Shahrokhian, S.; Panahi, S. Enhanced Electrochemical Activity of a Hollow Carbon Sphere/Polyaniline-Based Electrochemical Biosensor for Hbv DNA Marker Detection. *ACS Biomater. Sci. Eng.* **2019**, *5*, 2587–2594.

(36) Xiong, E.; Li, Z.; Zhang, X.; Zhou, J.; Yan, X.; Liu, Y.; Chen, J. Triple-Helix Molecular Switch Electrochemical Ratiometric Biosensor for Ultrasensitive Detection of Nucleic Acids. *Anal. Chem.* **2017**, *89*, 8830–8835.

(37) Hu, Q.; Su, L.; Huang, Y.; Chen, Z.; Cao, X.; Luo, Y.; Qin, D.; Niu, L. Coenzyme-Mediated Electro-Grafting for Ultrasensitive Electrochemical DNA Biosensing. *Sens. Actuators, B* **2021**, *346*, 130551–130558.

(38) Ahn, S. Y.; Liu, J.; Vellampatti, S.; Wu, Y.; Um, S. H. DNA Transformations for Diagnosis and Therapy. *Adv. Funct. Mater.* **2020**, *31*, No. 2008279.

(39) Moccia, M.; Antonacci, A.; Saviano, M.; Caratelli, V.; Arduini, F.; Scognamiglio, V. Emerging Technologies in the Design of Peptide Nucleic Acids (Pnas) Based Biosensors. *TrAC, Trends Anal. Chem.* **2020**, *132*, No. 116062.

(40) Liu, Q.; Liu, J.; Yang, H.; Wang, X.; Kong, J.; Zhang, X. Highly Sensitive Lung Cancer DNA Detection Via Go Enhancing Eatrps Signal Amplification. *Microchem. J.* **2021**, *160*, No. 105766.

(41) Lo, Y.; Cheung, Y. W.; Wang, L.; Lee, M.; Figueroa-Miranda, G.; Liang, S.; Mayer, D.; Tanner, J. A. An Electrochemical Aptamer-Based Biosensor Targeting Plasmodium Falciparum Histidine-Rich Protein Ii for Malaria Diagnosis. *Biosens. Bioelectron.* **2021**, *192*, No. 113472.

(42) Iliuk, A. B.; Hu, L.; Tao, W. A. Aptamer in Bioanalytical Applications. *Anal. Chem.* **2011**, *83*, 4440–4452.

(43) Genereux, J. C.; Barton, J. K. Mechanisms for DNA Charge Transport. *Chem. Rev.* **2010**, *110*, 1642–1662.

(44) Rossetti, M.; Brannetti, S.; Mocenigo, M.; Marini, B.; Ippodrino, R.; Porchetta, A. Harnessing Effective Molarity to Design an Electrochemical DNA-Based Platform for Clinically Relevant Antibody Detection. *Angew. Chem., Int. Ed.* **2020**, *59*, 14973–14978.

(45) Abedi, R.; Raoof, J. B.; Hashkavayi, A. B.; Asghary, M. Highly Sensitive and Label-Free Electrochemical Biosensor Based on Gold Nanostructures for Studying the Interaction of Prostate Cancer Gene Sequence with Epirubicin Anti-Cancer Drug. *Microchem. J.* **2021**, *170*, No. 106668.

(46) Cash, K. J.; Ricci, F.; Plaxco, K. W. An Electrochemical Sensor for the Detection of Protein-Small Molecule Interactions Directly in Serum and Other Complex Matrices. *J. Am. Chem. Soc.* **2009**, *131*, 6955–6957.

(47) Wu, L.; Qi, P.; Fu, X.; Liu, H.; Li, J.; Wang, Q.; Fan, H. A Novel Electrochemical Pcb77-Binding DNA Aptamer Biosensor for Selective Detection of Pcb77. *J. Electroanal. Chem.* **2016**, *771*, 45–49.

(48) Das, J.; Gomis, S.; Chen, J. B.; Yousefi, H.; Ahmed, S.; Mahmud, A.; Zhou, W.; Sargent, E. H.; Kelley, S. O. Reagentless Biomolecular Analysis Using a Molecular Pendulum. *Nat. Chem.* **2021**, *13*, 428–434.

(49) Cash, K. J.; Plaxco, K. W. Signal Transduction with a Swing. *Nat. Chem.* **2021**, *13*, 392–393.

(50) Clifford, A.; Das, J.; Yousefi, H.; Mahmud, A.; Chen, J. B.; Kelley, S. O. Strategies for Biomolecular Analysis and Continuous Physiological Monitoring. *J. Am. Chem. Soc.* **2021**, *143*, 5281–5294.